Multi-instrument observations of SED during 24–25 October 2011 storm: Implications for SED formation processes

Shasha Zou,[1] Aaron J. Ridley,[1] Mark B. Moldwin,[1] Michael J. Nicolls,[2] Anthea J. Coster,[3] Evan G. Thomas,[4] and J. Michael Ruohoniemi[4]

[1]   We present multiple instrument observations of a storm-enhanced density (SED) during the 24–25 October 2011 intense geomagnetic storm. Formation and the subsequent evolution of the SED and the midlatitude trough are revealed by global GPS vertical total electron content maps. In addition, we present high time resolution Poker Flat Incoherent Scatter Radar (PFISR) observations of ionospheric profiles within the SED. We divided the SED observed by PFISR into two parts. Both parts are characterized by elevated ionospheric peak height (h_mF_2) and total electron content, compared to quiet time values. However, the two parts of the SED have different characteristics in the electron temperature (T_e), the F region peak density (N_mF_2), and convection flows. The first part of the SED is associated with enhanced T_e in the lower F region and reduced T_e in the upper F region and is collocated with northward convection flows. The N_mF_2 was lower than quiet time values. The second part of the SED is associated with significantly increased N_mF_2, elevated T_e at all altitudes and is located near the equatorward boundary of large northwestward flows. Based on these observations, we suggest that the mechanisms responsible for the formation of the two parts of the SED may be different. The first part is due to equatorward expansion of the convection pattern and the projection of northward convection flows in the vertical direction, which lifts the ionospheric plasma to higher altitudes and thus reduces the loss rate of plasma recombination. The second part is more complicated. Besides equatorward expansion of the convection pattern and large upward flows, evidences of other mechanisms, including horizontal advection due to fast flows, energetic particle precipitation, and enhanced thermospheric wind in the topside ionosphere, are also present. Estimates show that contribution from precipitating energetic protons is at most ~10% of the total F region density. The thermospheric wind also plays a minor role in this case.

1.   Introduction

[2]   Space weather effects of ionosphere variability are important magnetosphere-ionosphere-thermosphere coupling science topics. The impact of solar wind energy on geospace is of particular importance during geomagnetic storms. During a geomagnetic storm, a ridge of electron density enhancement often occurs in the mid-latitude and subauroral region, named storm-enhanced density (SED) [*Foster*, 1993]. Occasionally, SED extends to higher latitudes, into the cusp and the polar cap, where it is termed tongue-of-ionization (TOI). The density enhancements of SED/TOI can be extremely large and localized, with steep density gradients and irregularities developing at their boundaries, in particular the boundary between the SED and the mid-latitude trough further poleward. These steep gradients can cause severe disruptions in radio communication and navigation systems [*Ledvina et al.*, 2002; *Doherty et al.*, 2004; *Skone et al.*, 2004; *Coster and Skone*, 2009; *Sun et al.*, 2013]. Therefore, the formation of the SED/TOI and their evolution under the influence of the interplanetary magnetic field (IMF) and solar wind variations are under intense study. Comprehensive local and global-scale observations are necessary for understanding SED formation and evolution. The rapid increasing

Additional supporting information may be found in the online version of this article.

[1]Department of Atmospheric, Oceanic and Space Sciences, University of Michigan, Ann Arbor, Michigan, USA.

[2]Center for Geospace Studies, SRI International, Menlo Park, California, USA.

[3]Haystack Observatory, Massachusetts Institute of Technology, Westford, Massachusetts, USA.

[4]Department of Electrical and Computer Engineering, Virginia Tech, Blacksburg, Virginia, USA.

Corresponding author: S. Zou, Department of Atmospheric, Oceanic and Space Sciences, University of Michigan, Ann Arbor, MI 48109–2143, USA. (shashaz@umich.edu)

number of GPS receivers over the globe enables imaging the ionospheric total electron content (TEC) on a global scale [*Mannucci et al.*, 1998; *Rideout and Coster*, 2006]. This TEC imaging capability can clearly reveal the evolution of these ionospheric density structures and thus renewed the interest of SED/TOI studies [*Foster et al.*, 2005]. In addition, ground-based incoherent scatter radars are able to reveal the characteristics of altitude profiles of ionospheric parameters and convection flows within SED/TOI. These characteristics often include elevated F region TEC, increased ionospheric F_2 layer peak density height (h_mF_2), low electron temperature (T_e), and large sunward convection flows [*Foster et al.*, 2005; *Huang et al.*, 2005]. SED and TOI are believed to play an important role in supplying F region plasma to the polar area and auroral region in the nightside [*Foster et al.*, 2005]. Moreover, the recent expansion of Super Dual Auroral Radar Network (SuperDARN) high frequency radar coverage to mid-latitudes has made it possible to monitor the equatorward expansion of global convection even during strongly disturbed periods [e.g., *Clausen et al.*, 2012; *Thomas et al.*, 2013].

[3] A few different mechanisms have been suggested to account for the formation of SED. A snowplow effect model has been suggested by *Foster* [1993]: The expanding convection cells continuously encounter fresh solar-produced plasma at its equatorward edge and produce a latitudinally narrow region of SED. This enhanced density is then transported poleward along convection trajectories to higher latitude and form a plume-like feature. When it enters the polar region, it becomes the TOI. The large sunward convection flows often observed to accompany the SED are suggested to be subauroral polarization streams (SAPS) [*Foster and Burke*, 2002; *Foster and Vo*, 2002]. The SAPS flows have been explained to be related to the Region-2 current system formation [*Erickson et al.*, 1991; *Zou et al.*, 2009a, 2009b, 2012; *Gkioulidou et al.*, 2009, 2011] and map to a low-conductance region, i.e., the mid-latitude trough, in the ionosphere. They have been shown to have significant space weather impact [e.g., *Coster and Foster*, 2007]. Since the SED is associated with density enhancement while the SAPS are expected to occur in a low-density region, *Fuller-Rowell* [2011] commented that these two explanations seem to contradict each other.

[4] An enhanced fountain effect has also been suggested to be able to lead to SED formation during superstorms ($Dst <$ -250 nT) [*Tsurutani et al.*, 2004; *Mannucci et al.*, 2005]. That is equatorial F region plasma that has been carried to higher altitudes by large E × B drift diffuses to higher latitudes along the magnetic field and contributes to the enhanced TEC in the SED. The density peak is usually found to be located at ~±25° to 40° magnetic latitude (MLAT) [*Tsurutani et al.*, 2013]. *Kelley et al.* [2004] presented a simple quantitative calculation of SED and argued that in addition to the enhanced equatorial fountain effect, the westward flows that transport enhanced density from the duskside to the dayside also contribute to the density buildup in SED.
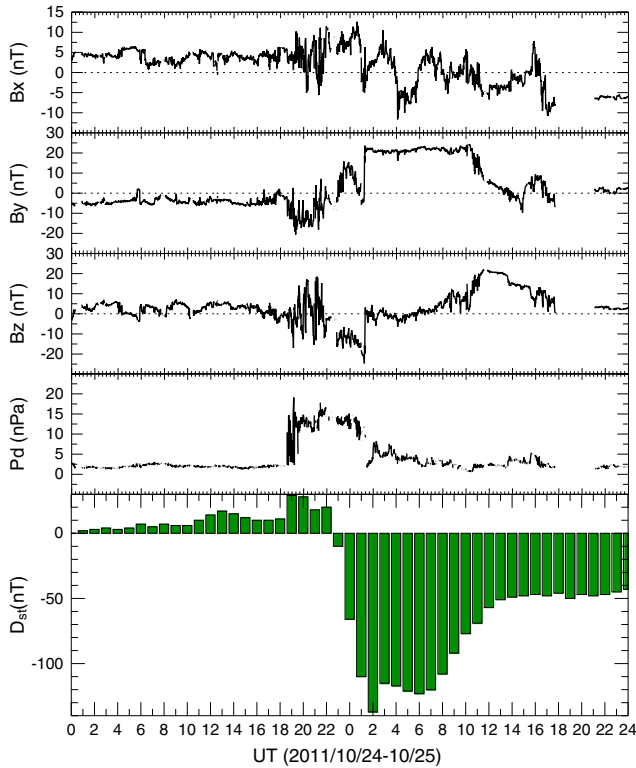
[5] Based on a detailed event study, *Huang et al.* [2005] argued that the enhanced fountain effect cannot account for the SED formation at relatively higher latitudes, such as over Millstone Hill located at ~53° MLAT. They suggested that penetrating eastward electric fields and thus poleward flows were responsible for the density enhancement over Millstone Hill during that storm. *Deng and Ridley* [2006]

investigated the ionospheric reactions to a 20 nT southward turning of IMF B_z and found enhancements in both N_mF_2 and TEC and signatures of TOI. They attributed these changes to enhanced vertical flows on the dayside. More specifically, the northward component of the convection flows near noon has a vertical velocity component, due to the nonvertical magnetic field. This vertical velocity can lift the plasma up to regions with lower recombination rates and thus increase the electron density. *Heelis et al.* [2009] used the Utah State University Time Dependent Ionospheric Model (TDIM) and suggested that SED can be due to the equatorward expansion of the high-latitude magnetospheric convection pattern. They emphasized a local enhancement of density instead of transport effects due to large convection flows, although both of them are features of enhanced convection. As a step forward, *David et al.* [2011] used TDIM coupled with the University of Michigan's Hot Electron and Ion Drift Integrator to study the storm time convection electric field in producing the SED observed during the 7–8 September 2002 storm. They found that a magnetospheric electric field with an eastward component that penetrates to mid-latitudes increases local production on the dayside to a degree that is sufficient to account for the SED. *Thomas et al.* [2013] recently examined two cases of SED structures to demonstrate the controlling role of convection electric field in determining whether the SED may form a TOI or instead persist as an inactive "fossil" feature.

[6] The thermospheric wind can also affect the dayside TEC. During active times, the thermospheric expansion at the auroral zone produces enhanced equatorward winds. This equatorward wind will reduce or even overcome the poleward wind predominant during quiet times. If a net equatorward wind exists, it would induce an upward ion drift along the magnetic field line. The thermospheric wind may lag the onset of the storm by several hours. *Lu et al.* [2012] performed a comprehensive modeling study of the role of electric fields and disturbance meridional winds in lifting ionospheric ions for the 9 November 2004 storm. They found that the disturbance meridional winds played a more important role than the electric field at mid-latitudes in that storm.

[7] In past literature, SED has been widely used to describe the TEC enhancements in the mid-latitudes (i.e., inner-plasmasphere field lines) as well as those at higher latitudes (i.e., outer-plasmasphere field lines), including the plume of ionization that extend to higher latitudes. *Foster et al.* [2007] refined the definition of SED as disturbance-enhanced TEC entrained in the sunward convection within either the plasmasphere boundary layer or within the plumes and their extension into the polar cap. In this work, the SED phenomena targeted is consistent with the definition in *Foster et al.* [2007].

[8] As pointed out by *Fuller-Rowell* [2011], the details of the SED feature require further study. In this paper, we present an event study of the formation of SED during a geomagnetic storm on 24–25 October 2011 using multiple instrument observations. This storm was induced by a coronal mass ejection. High time resolution Poker Flat Incoherent Scatter Radar (PFISR) observations during this period enable us to investigate the rapid response of the dayside ionospheric properties to the IMF and solar wind changes. We present observations of important ionospheric parameters, such as the F_2 layer

Figure 1. Propagated solar wind and IMF observations for 24 and 25 October 2011. From top to bottom, magnetic field components B_x, B_y, and B_z in GSM coordinates, solar wind dynamic pressure (P_d), and Dst are shown.

density peak (N_mF_2) and height (h_mF_2), TEC, and altitude profiles of those parameters within the SED and its boundary, and discuss possible mechanisms responsible for the formation of SED in this case.
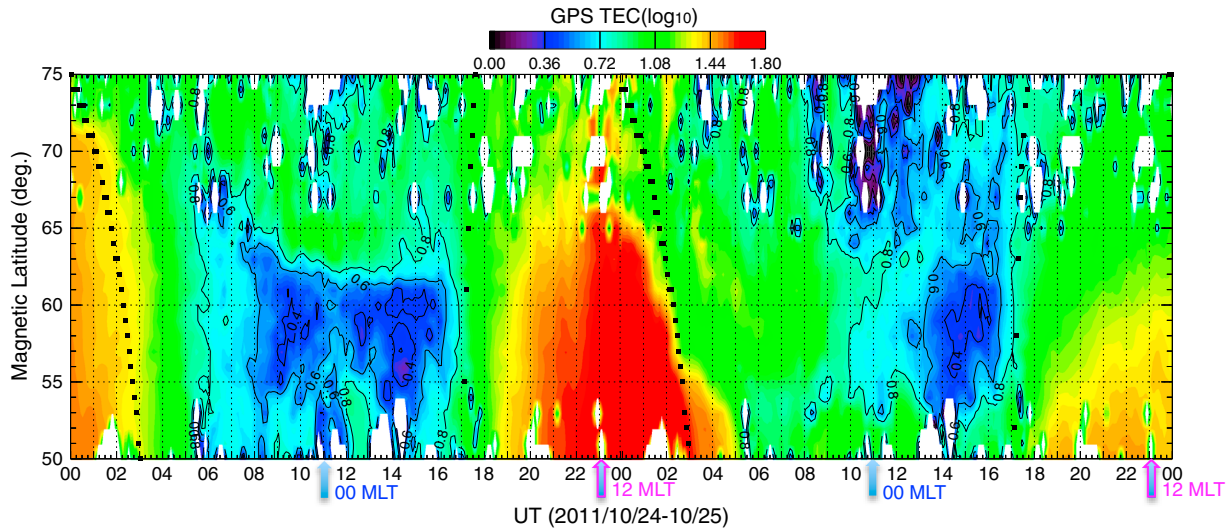
2. Observations

[9] Figure 1 shows the solar wind observations from 24 October to 25 October 2011, as well as the Dst index. The solar wind data are obtained from the OMNIweb and have been propagated to the Earth's bow shock nose. From top to bottom, three magnetic field components B_x, B_y, and B_z in GSM coordinates, solar wind dynamic pressure (P_d), and D_{st} are shown. The solar wind dynamic pressure increased at ~1840 UT on 24 October by a factor of 5, which was followed by large-amplitude fluctuations in the magnetic field. Significant (10–20 nT) IMF B_z fluctuations were observed beginning at ~1900 UT on 24 October. At ~2200 UT on 24 October, the IMF B_z became largely southward and remained southward for about 3 h. At the same time as the southward turning, the IMF B_y turned from strongly negative to strongly positive. After ~0120 UT on 25 October, the IMF B_z started to fluctuate around zero and IMF B_y around 20 nT with small amplitudes, while the solar wind dynamic pressure gradually dropped back to quiet time values. An intense geomagnetic storm occurred due to the above solar wind conditions. The storm sudden commencement triggered by the dynamic pressure enhancement and marked the beginning of the storm at ~1900 UT. The D_{st} minimum exceeded ~ −130 nT during this intense storm.

[10] Selected 2-D GPS vertical total electron content (VTEC) maps during this storm are displayed in Figure 2, together with ionospheric equipotential contours derived from the SuperDARN radar observations. The SuperDARN convection patterns are derived in the corotating reference frame. The contours represent streamlines of plasma convection and the contour maps are obtained by fitting the distribution of line-of-sight velocity data from the SuperDARN radars to an expansion of the electrostatic potential in terms of spherical harmonic functions as described by *Ruohoniemi and Baker* [1998] and *Shepherd and Ruohoniemi* [2000]. The VTEC data are processed at the Haystack Observatory of Massachusetts Institute of Technology at 5 min resolution from a global network of GPS receivers and can be accessed via the Madrigal database [*Rideout and Coster*, 2006]. Using a standard spatiotemporal median filtering technique, data from three consecutive intervals are used to generate a single map of GPS VTEC as described by *Thomas et al.* [2013]. These maps are available for plotting from the Virginia Tech SuperDARN website. Both maps are shown in magnetic local time (MLT) and geomagnetic latitude (MLAT) coordinates. In each panel, 12 MLT/0 MLT is at the top/bottom. It is important to note that no GPS VTEC data are plotted above 85° MLAT due to limitations in the median filtering process. A movie from 1800 UT on 24 October to 0400 UT on 25 October is also provided as supporting information. Thick grey curves are drawn to roughly highlight the boundaries of the SED. The SED can be seen first in the noon-dusk sector over Canada in these maps. As the Earth rotates, the Alaska region, where PFISR is located, is shifted underneath the SED. Then PFISR is able to measure the detailed vertical profiles within the SED and these observations are shown in the later text. We divided the SED into two parts based on the ionospheric properties measured by PFISR, including convection flows within the SED, vertical density profile, and plasma temperature. Details of the PFISR observation are shown in Figures 6–11. The corresponding SED structures in GPS VTEC are also labeled in Figures 2d and 2h. The cross polar cap potential was generally increasing during this period although with fluctuations, indicated by the denser equipotential contours at later times due to the southward turning of the IMF B_z after 2200 UT on 24 October. In Figures 2d–2h, as the IMF B_z became further southward and the B_y component switched to positive, the convection pattern expanded further equatorward and the dusk cell was much larger than the dawn cell. The convection throat on the dayside also shifted toward the dawnside. The mid-latitude ionospheric trough, as a longitudinally extended low TEC channel, formed and deepened underneath the westward convection flows of the expanding dusk convection cell. These westward flows carried the mid-latitude trough into the noon sector. Note the high degree of alignment between the equatorward edge of the trough feature and the most equatorward convection contour of Figure 2h. This feature has also been observed in *Zhang et al.* [2013].

[11] Figure 3 shows the time series of GPS VTEC at −96° geomagnetic longitude (mlon) over central Alaska from 50° to 75° MLAT for these 2 days. For a given time, data points at the same latitudes and within 3° centered at this mlon are averaged. This longitude is chosen because this is where PFISR is located and the plot is shown mainly to provide a large-scale context for the PFISR observation presented in
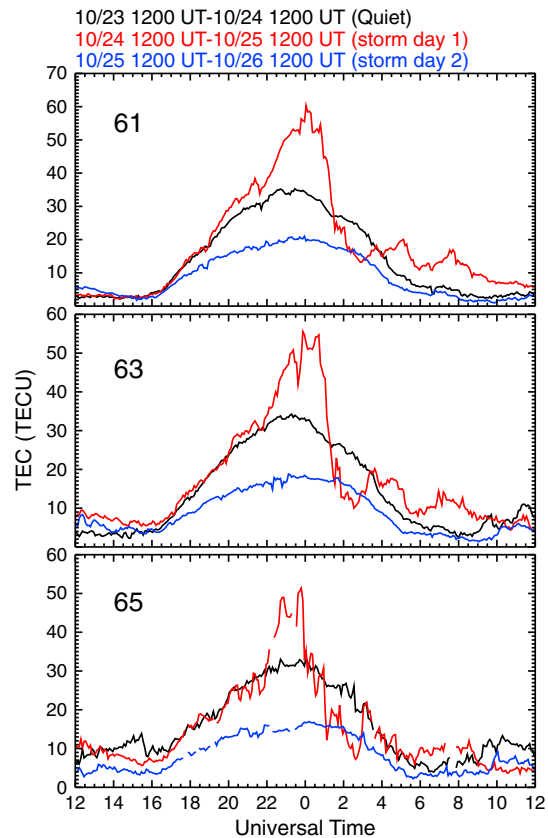
Figure 2. (a–h) Selected 2-D GPS VTEC maps during the main phase of the 24–25 October storm. Ionospheric equipotential contours derived from the SuperDARN radar observations are also shown. In each panel, magnetic noon/midnight is at the top/bottom, and dusk/dawn is toward the left/right. PFISR beams are also plotted as magenta segments.

Figure 6. Black squares denote the solar terminator at the surface of the Earth. The diurnal variation, i.e., high/low TEC during the day/night, and the storm-related signatures, such as the large TEC enhancement between 0000 and 0200 UT on 25 October compared with that between 0000 and 0200 UT on 24 October, are clearly revealed in this figure. The GPS VTEC around magnetic local noon (SED) was significantly enhanced during the storm time (e.g., 0000 UT/13 MLT on 25 October) than that during quiet time (e.g., 0000 UT/13 MLT on 24 October).

[12] Figure 4 shows quiet and storm time GPS VTEC at three different MLATs along the $-96°$ mlon. The black curve represents the quiet time value measured from 1200 UT on 23 October to 1200 UT on 24 October, while red and blue

Figure 3. Time series of GPS VTEC at central Alaska (−96° geomagnetic longitude) for 24 and 25 October 2011. Black squares denote the solar terminator. Magnetic local noon is at ~2305 UT at this longitude.
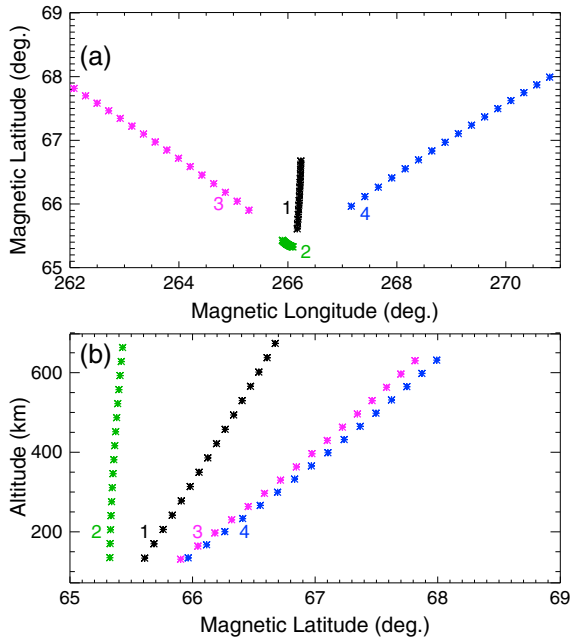
curvesare measured from 1200 UT on 24 October to 1200 UT on 25 October (storm day 1), and from 1200 UT on 25 October to 1200 UT on 26 October (storm day 2), respectively. After Alaska entered into sunlit region at ~1600 UT from the dawn and moving toward noon, the VTEC began to increase gradually for all 3 days. In general, the GPS VTEC was higher on the storm day 1 than it during quiet days. On the storm day 2, the GPS VTEC was lower than the quiet time value. In the early literature, when TEC was available from a fixed point or from a meridional chain, these features were named the ionospheric dusk effect [e.g., *Mendillo*, 2006]. We focus on the GPS VTEC observations during the storm day 1. After the dynamic pressure enhancement at ~1840 UT, the VTEC started to increase at a higher rate than that during the quiet time. This effect was clearer at lower latitude than that at higher latitude. Another rapid increase in the VTEC (~20 total electron content unit (TECU) per hour, 1 TECU $= 10^{16}$ el m^{-2} initiated at all latitudes at ~2200 UT, i.e., the time of IMF southward turning. The peak of the VTEC was about 60 TECU at 61° MLAT and 50 TECU at 65° MLAT, which are ~70% and ~53% higher than the quiet time value, respectively. The peak was followed by a sharp decrease and the local dip around 0300 UT was even lower than the quiet time value by ~10–18 TECU. Based on Figure 3, this VTEC decrease was due to the intrusion of the mid-latitude trough into the noon sector.

[13] PFISR was operated in an international polar year four-beam mode during this period [*Sojka et al.*, 2009]. The beam configuration is shown in Figure 5. Beam 2 is located at the lowest latitude roughly pointing along the local magnetic field line. Beam 1 is pointing toward magnetic north (geographically vertical), and beams 3 and 4 are pointing northwestward and northeastward, respectively. Figure 6 shows the PFISR observations from 1300 UT on 24 October to 0400 UT on 25 October (Figures 6a–6e) during the storm day 1 and the same UT range of a quiet period (Figures 6f–6j), which is shown for comparison. The convection flow direction (Figures 6a and 6f), magnitude

(Figures 6b and 6g), vector (Figures 6c and 6h), and the electron density profiles from beam 4 (Figures 6d and 6i) and beam 2 (Figures 6e and 6j) are shown. During the quiet period, the magnitude of the convection flows were very small at these latitudes and the electron densities observed by all

Figure 4. GPS VTEC values at three different magnetic latitudes for storm day 1 (red), storm day 2 (blue), and a quiet day (black).
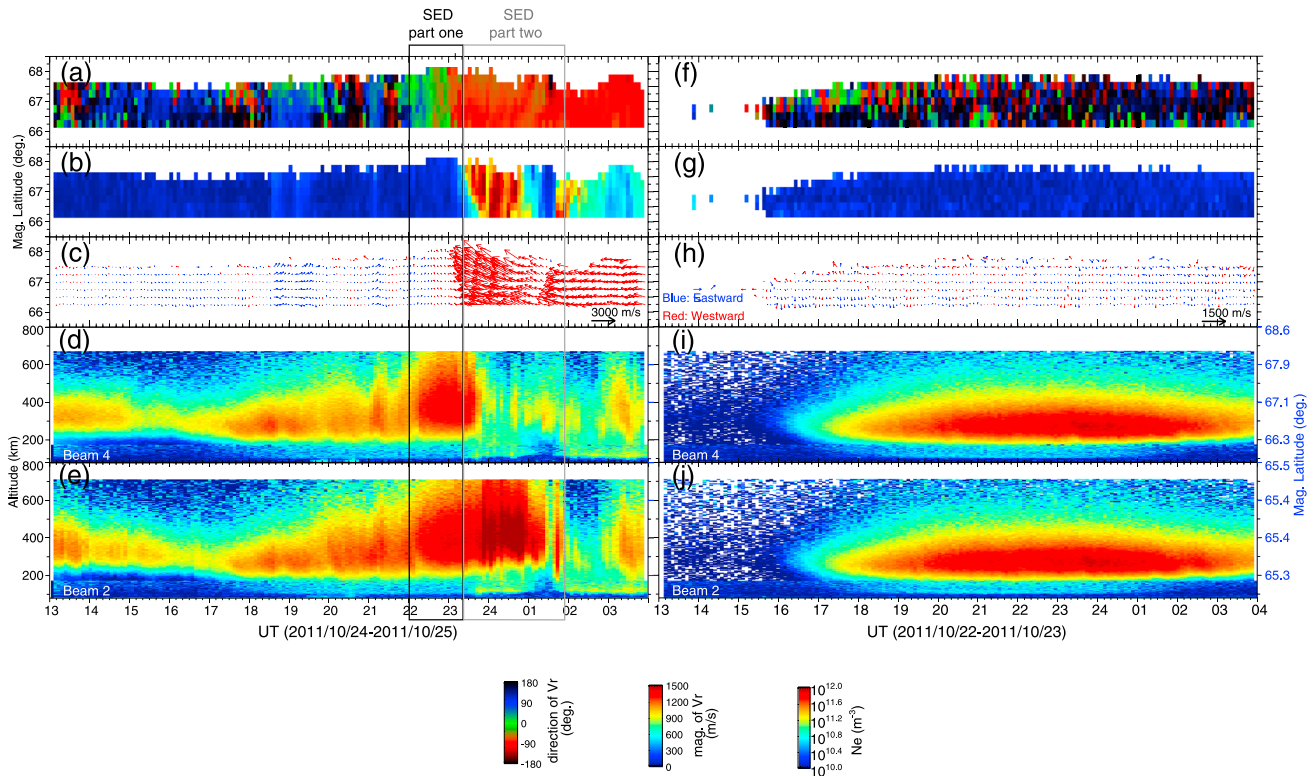
Figure 5. PFISR beam configuration in geomagnetic coordinates during this radar run.

four PFISR beams (two beams shown here) show typical diurnal variations. In contrast, considerable variations in the plasma convection and electron density can be seen during the storm period. Several important features in Figure 6 are discussed below.
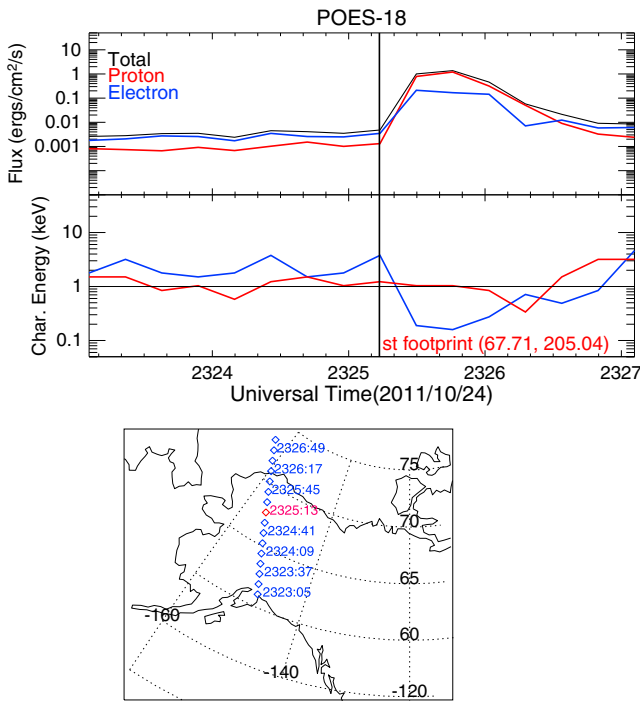
[14] The solar wind dynamic pressure increased at ~1840 UT. Plasma convection speed (Figures 6b and 6c) increased by a couple of 100 m/s. The h_mF_2 was slightly elevated from the quiet time value after ~1900 UT, while the N_mF_2 was lower than quiet time values.

[15] Between 2200 UT and 2320 UT on 24 October, a large F region electron density enhancement can be seen in both beams and the enhanced density extended up to the upper altitude limit of PFISR. The corresponding h_mF_2 increased ~70–110 km and the N_mF_2 increased by ~5×10^{11} m^{-3}. Meanwhile, northward convection flows were observed by PFISR during this period in Figures 6a and 6c. We name this density enhancement as the first part of the SED. As shown in Figure 2d, this part of SED extended antisunward toward the polar cap.

[16] The northward convection flows terminated at ~2320 UT on 24 October and were followed by large northwestward flows. The convection flows first increased at higher latitude and then moved to lower latitude, as a signature of the polar
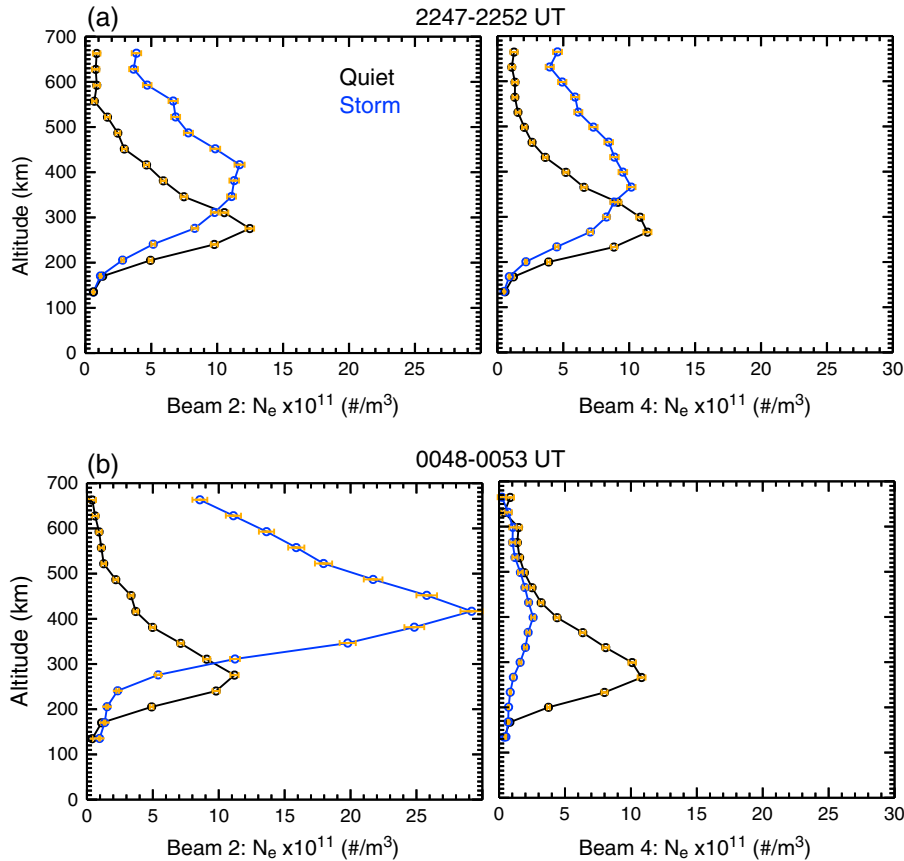

Figure 6. (a–e) PFISR observations of ionospheric convection and electron density from 1300 UT on 24 October to 0400 UT on 25 October 2011. From top to bottom, the convection flow direction (Figure 6a), magnitude (Figure 6b), and vector (Figure 6c), the electron density profiles from beam 4 (Figure 6d) and beam 2 (Figure 6g) are shown. Convection flow data are plotted only if the measurement uncertainty is less than 150 m/s. The direction of the flow is zero if pointing to the magnetic north and increases (decreases) clockwise (counterclockwise). Convection flows with eastward/westward component are blue/red. (f–j) PFISR observations of ionospheric convection and electron density from 1300 UT on 22 October to 0400 UT on 23 October 2011. The observations are obtained during geomagnetic quiet time and are shown for comparison purpose.
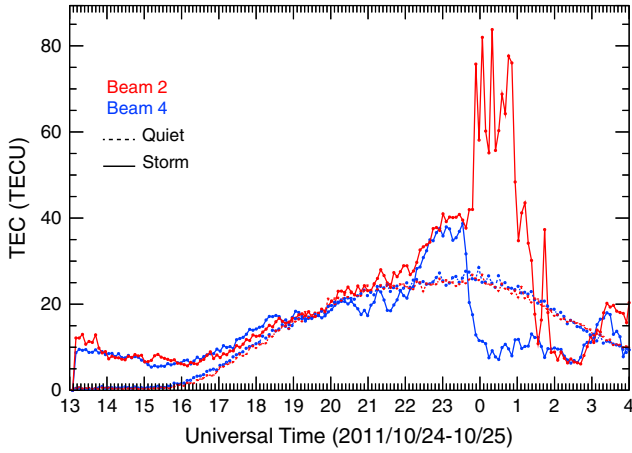
Figure 7. POES-18 satellite observation of the precipitating particle fluxes and characteristic energy from 2323 to 2327 UT on 24 October 2011. The satellite trajectory is also shown.

cap expansion, consistent with the gradually increasing southward IMF. At the same time, largely reduced electron densities were observed by beam 4 at higher latitudes, while further elevated electron densities are observed by beam 2 at the lowest latitudes. Together with Figures 2g and 2h, it is clear that this further density enhancement observed by beam 2 occurred within the second part of the SED. In this case, the narrow SED plume extended nearly azimuthally from the postnoon sector to the prenoon sector. The low electron density was observed by beam 2 later after ~0200 UT on 25 October. Comparing with the GPS VTEC map, it is revealed that the low-density region measured by PFISR was the mid-latitude trough.

[17] Figure 7 shows POES-18 satellite observations of the energy flux and characteristic energies of precipitating particles, red for proton and blue for electron. The satellite trajectory is also shown. POES-18 was moving from lower to higher latitudes over Alaska from 2323 UT to 2327 UT. The energy flux was contributed predominately from energetic protons and the characteristic energy of electron flux was only ~100–200 eV. In addition, Active Magnetosphere and Planetary Electrodynamics Response Experiment (AMPERE) observations during these periods (not shown) also indicate that PFISR was located within downward Region-2 sense field-aligned current region. These observations provide some evidence that the large westward flows are probably SAPS. The ionization caused by energetic proton precipitation is

Figure 8. Comparisons of electron density vertical profiles under quiet (black line) and storm (blue) conditions at (a) 2247–2252 UT, during the first part of the SED, and (b) 0048–0053 UT, during the second part of the SED.
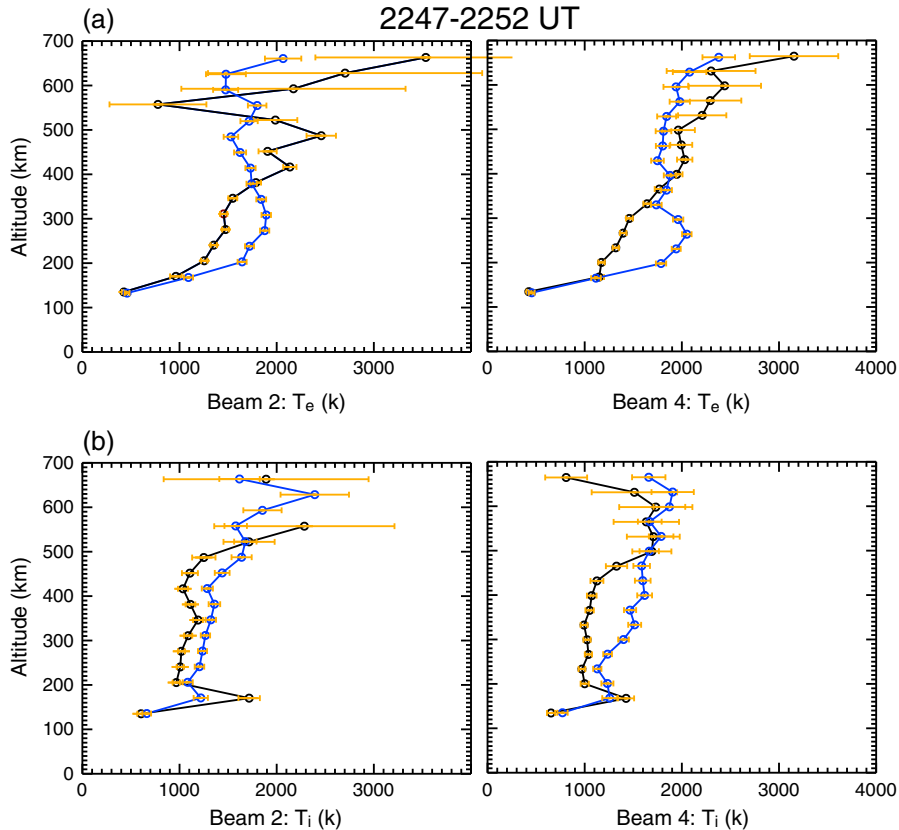
Figure 9. TEC value at beams 2 and 4 calculated by integrating the PFISR density profile from ~116 km to ~692 km.
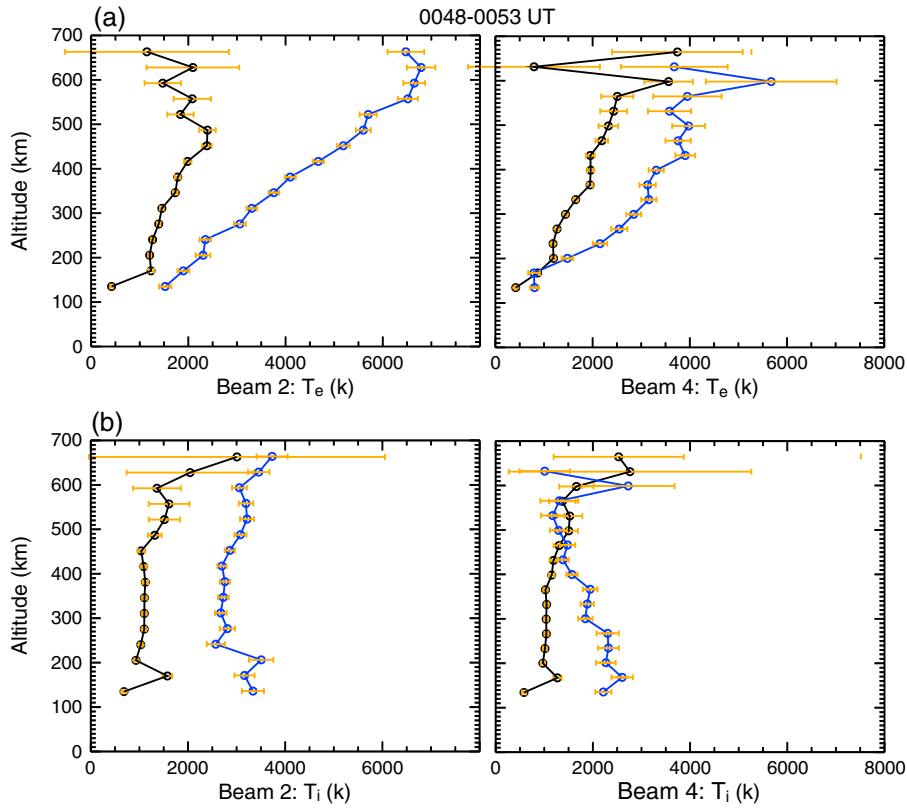
[18] Figure 8 shows comparisons of electron density vertical profiles under quiet (black line) and storm (blue) conditions at two selected epochs, while Figure 9 displays the TEC value at beams 2 (red) and 4 (blue) calculated by integrating the density profile from ~116 km to ~692 km during quiet (dashed lines) and storm time (solid lines). Figure 8a shows the electron density vertical profile at ~2250 UT on 24 October, which was about 50 min after the IMF B_z southward turning and during northward convection flows period. Below ~300 km, storm time electron density decreased compared with the quiet time value. In contrast, above 300 km, the electron density increased significantly (~2–3 times) during storm time. This topside ionospheric electron density increase accounts for the GPS VTEC increase in Figure 4 and the incoherent scatter radar (ISR) TEC in Figure 9.

[19] The electron density vertical profile at ~0050 UT on 25 October is shown in Figure 8b, which was during the large northwestward convection flows. The N_mF_2 measured by beam 2 reached ~3×10^{12} m^{-3}, nearly triple the quiet time value, and the peak height was lifted up to ~420 km, roughly 140 km higher than the quiet time value. The electron density in the mid-latitude trough was measured by beam 4. It is much lower than the quiet time value at all altitudes and the vertical profile was almost flat with the F region peak barely detectable. The N_mF_2 dropped back to ~1–2×10^{11} m^{-3}, while the h_mF_2 remained elevated at ~400 km. The drastically different electron density profiles observed by beams 2 and 4 during northwestward flows are consistent with the observed dramatic TEC gradient. In Figure 9, the TEC spikes

also evident in the E region electron density between 2320 UT on 24 October and 0400 UT on 25 October in Figures 6d and 6e. Ionizations due to energetic precipitating protons have been reported to be more effective in ionizing the E region rather than the F region [e.g., *Galand and Richmond*, 2001; *Deng et al.* 2013]. Based on the E region density enhancement, we calculated an upper limit of the F region density enhancement due to these precipitating protons and found that their maximum contribution is ~10%.

Figure 10. Comparisons of (a) electron temperature and (b) ion temperature vertical profiles under quiet (black line) and storm (blue) conditions at 2247–2252 UT on 24 October 2011, during the first part of the SED.
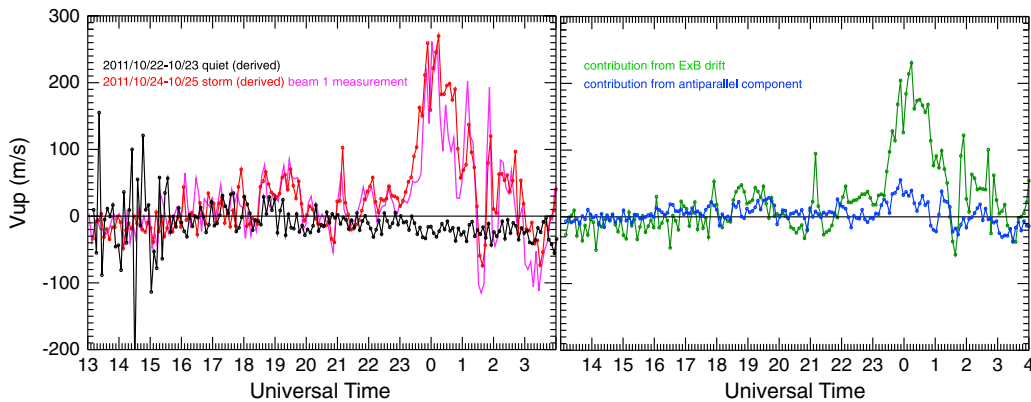
Figure 11. Comparisons of (a) electron temperature and (b) ion temperature vertical profiles under quiet (black line) and storm (blue) conditions at 0048–0053 UT on 25 October 2011, during the second part of the SED.
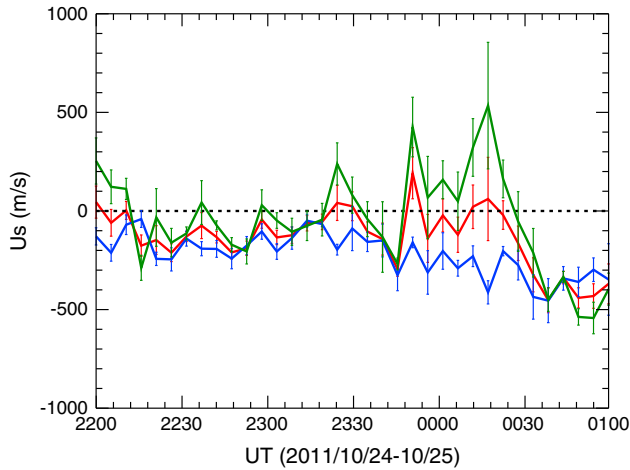
calculated from beam 2 measurements between 0000 UT and 0100 UT on 25 October reached ~80 TECU, ~50 TECU higher than quiet time value at this location/time. At the same time, the TEC dips at beam 4 were ~10 TECU, ~15–20 TECU lower than quiet time and comparable to nighttime values. Comparing the TEC spikes and dips observed by beams 2 and 4, the TEC gradient was on the order of 70 TECU within less than two geomagnetic degrees.

[20] Figures 10 and 11 show electron temperature (T_e) and ion temperature (T_i) vertical profiles measured by PFISR beams 2 and 4 at ~2250 UT on 24 October and ~0050 UT on 25 October. In Figure 10, above the F region density peak (~320 km), T_e during storm time was lower than that during quiet time. The opposite is true for T_e below the F region density peak. However, storm time T_i was in general higher than the quiet time value due to ion-neutral frictional heating. Different T_e and T_i behavior has been reported before by *Huang et al.* [2005]. However, in their case, T_e within the enhanced density structure was lower than that during quiet time at all altitudes measured by the Millstone radar. In

Figure 12. (a) Vertical flows derived from PFISR observation during storm (red) and quiet (black) time. Beam 1 is pointing toward magnetic north (geographically vertical). (b) Contribution of the vertical flows from $E \times B$ convection flows and antiparallel component measured along the magnetic field line during storm time.

Figure 13. Meridional thermospheric wind estimation, positive southward, from PFISR measurements between 2200 UT on 24 October and 0100 UT on 25 October 2011. Error bars represent standard error.

Figure 11, during the northwestward convection flow period, both electron and ion temperatures increased significantly with a larger magnitude at beam 2 than those at beam 4.

3. Discussion

[21] In this section, we discuss possible mechanisms that are responsible for the formation of the SED in this case. The two episodes of enhanced densities show different characteristics, suggesting the presence of different mechanisms.

[22] The first density increase observed between ~2200 UT and ~2320 UT on 24 October was accompanied with moderate northward convection flows, reduced T_e in the topside ionosphere, and enhanced T_e in the lower F region. As known for many years, northward convection flows could lift the F region plasma upward to regions with lower recombination rate, given a nonvertical local magnetic field line. At the location of PFISR, the geomagnetic field dip angle is ~77.7° based on the International Geomagnetic Reference Field (IGRF) 2010 model. Figure 12a shows the vertical flow derived from the PFISR observation during storm time (red) and quiet time (black) using the method described in *Heinselman and Nicolls* [2008]. Direct measurement from beam 1 (the vertical beam) is also shown in Figure 12a as a magenta curve. The similarity between the magenta and the red curves further confirms the validity of the velocity vector derivation method in *Heinselman and Nicolls* [2008]. Contributions from the $E \times B$ drift (green) and the antiparallel flow (blue) to the vertical flows are separated and shown in Figure 12b. Between 2200 UT to 2320 UT, the vertical flow was on the order of a few tens m/s and was mainly due to the projection of the $E \times B$ drift. The T_e decrease/increase in the region of enhanced/reduced density is because, in the absence of heat source, the electron cooling rate is proportional to the electron density. Figure 13 shows an estimation of the equatorward thermosphere wind from 2200 UT to 0100 UT, averaged between 135 km and 522 km (red). Green and blue curves represent the average at higher (346–522 km) and lower altitude (135–310 km), respectively. The calculation of the thermosphere wind is based on the method

described in *Aponte et al.* [2005], under the assumption that the antiparallel flow is driven by equatorward thermosphere wind. Errors are large on this estimate because of the nearly vertical field line. During the first part of the SED (2200–2320 UT), the averaged wind is northward. Based on these observations, we suggest the first part of the SED is likely due to northward convection flow.

[23] The second density increase was observed by beam 2 between 2320 UT on 24 October and 0200 UT on 25 October. It was associated with large northwestward convection flows and significantly enhanced T_e and T_i. As suggested by POES-18 observations in Figure 12, these northwestward flows are probably SAPS. Together with Figure 2, these observations lend support to the scenario of the snowplow effect suggested by *Foster* [1993]. That is, the equatorward part of the SAPS flows during the enlarging convection cells encounters enhanced density in the poleward portion of the SED and transport them toward noon. Note that the majority of the SAPS was collocated with the mid-latitude trough. In addition, Figure 12b shows a large vertical velocity during this time as a combination of contributions from $E \times B$ convection flow and antiparallel flows with the former as the major source. These vertical flows lift the already enhanced seed population associated with first SED further upward and increase the density even more. As can be seen from Figure 13, the average wind was occasionally positive around 2400 UT and is mainly from the region above 350 km.

[24] Besides the above mechanism, there is also evidence of enhanced particle precipitation during the second part of the SED. However, it is not of major importance, because both beams 2 and 4 observed ionization due to those energetic particle precipitations, while only beam 2 observed the second part of the SED. In addition, the precipitating energy fluxes are not large enough to create such density enhancements based on *Galand and Richmond* [2001].

[25] The ion temperature increases within the fast flows are due to enhanced frictional heating, and would increase the recombination rate and thus lead to a decrease in the electron density. This effect probably contributes to the mid-latitude trough observed near the noon sector, in addition to the horizontal transport of low-density trough plasma from the nightside. It should also work against the enhanced production due to vertical lift of plasma but is not large enough to deplete the second part of the SED.

4. Summary and Conclusions

[26] We present multiple instrument observations of a SED during the intense geomagnetic storm occurred on 24–25 October 2011. Formation and the subsequent evolution of the SED and the mid-latitude trough are revealed by the global GPS VTEC maps. In addition, we present high time resolution PFISR observation of ionospheric profiles within the SED.

[27] The SED observed by PFISR are divided into two parts. Both parts are characterized by elevated ionospheric peak height (h_mF_2) and TEC, compared to the quiet time values. However, they have different characteristics in the electron temperature (T_e), the F region peak density (N_mF_2), and convection flows within the two parts of the SED. The first part of the SED is associated with enhanced T_e in the lower F region and reduced T_e in the upper F region and is collocated

with northward convection flows. The N_mF_2 was lower than quiet time value. The second part of the SED is associated with significantly increased N_mF_2, elevated T_e at all altitudes, and is located near the equatorward boundary of large northwestward convection flows. Based on these observations, we suggest that the mechanisms responsible for the formation of the two parts of the SED may be different. The first part is due to equatorward expansion of the convection pattern and the projection of northward convection flows in the vertical direction, which lifts the ionospheric plasma to higher altitude and thus reduces the loss rate of plasma recombination. The second part is more complicated. Besides the equatorward expansion of the convection pattern and large upward flows, other mechanisms are also involved, including horizontal advection due to fast flows, energetic particle precipitation, and enhanced thermospheric wind in the topside ionosphere. Estimation shows that contribution from precipitating energetic protons is at most ~10% of the total F region density. The enhanced thermospheric wind also plays a minor role in this case through contributing to the upward flows. The contribution of horizontal transport by fast flows cannot be quantified observationally and is under further investigation using numerical models.

[28] PFISR also measured a significant density and TEC gradient at the boundary of the second part of the SED and the mid-latitude trough. The trough extended from the nightside to the noon sector. This extended longitudinal coverage of the midlatitude trough is attributed to the unusually large positive IMF B_y in this case. This large IMF B_y also led to an early termination of the SED in terms of the MLT.

References

Aponte, N., M. J. Nicolls, S. A. Gonza´lez, M. P. Sulzer, M. C. Kelley, E. Robles, and C. A. Tepley (2005), Instantaneous electric field measurements and derived neutral winds at Arecibo, *Geophys. Res. Lett.*, 32, L12107, doi:10.1029/2005GL022609.

Clausen, L. B. N., et al. (2012), Large-scale observations of a subauroral polarization stream by midlatitude SuperDARN radars: Instantaneous longitudinal velocity variations, *J. Geophys. Res.*, 117, A05306, doi:10.1029/2011JA017232.

Coster, A., and J. Foster (2007), Space-weather impact of the subauroral polarization stream, *Radio Sci. Bull.*, 321, 28–36.

Coster, A., and S. Skone (2009), Monitoring storm-enhanced density using IGS reference station data, *J. Geod.*, 83(3–4), 345–351.

David, M., J. J. Sojka, R. W. Schunk, M. W. Liemohn, and A. J. Coster (2011), Dayside midlatitude ionospheric response to storm time electric fields: A case study for 7 September 2002, *J. Geophys. Res.*, 116, A12302, doi:10.1029/2011JA016988.

Deng, Y., and A. J. Ridley (2006), Role of vertical ion convection in the high-latitude ionospheric plasma distribution, *J. Geophys. Res.*, 111, A09314, doi:10.1029/2006JA011637.

Deng, Y., T. Fuller-Rowell, A. Ridley, D. Knipp, and R. Lopez (2013), Primary heating mechanisms for the substantial neutral density enhancements in the cusp region, *J. Geophys. Res. Space Physics*, 118, 1–10, doi:10.1002/jgra.50197.

Doherty, P., A. J. Coster, and W. Murtagh (2004), Space weather effects of October–November 2003, *GPS Solutions*, 8, 267–271.

Erickson, G. M., R. W. Spiro, and R. A. Wolf (1991), The physics of the Harang discontinuity, *J. Geophys. Res.*, 96, 1633–1645, doi:10.1029/90JA02344.

Foster, J. C. (1993), Storm time plasma transport at middle and high latitudes, *J. Geophys. Res.*, 98, 1675–1689, doi:10.1029/92JA02032.

Foster, J. C., and W. J. Burke (2002), SAPS: A new characterization for sub-auroral electric fields, *Eos Trans. AGU*, 83, 393.

Foster, J. C., and H. B. Vo (2002), Average characteristics and activity dependence of the subauroral polarization stream, *J. Geophys. Res.*, 107(A12), 1475, doi:10.1029/2002JA009409.

Foster, J. C., et al. (2005), Multiradar observations of the polar tongue of ionization, *J. Geophys. Res.*, 110, A09S31, doi:10.1029/2004JA010928.

Foster, J., W. Rideout, B. Sandel, W. Forrester, and F. Rich (2007), On the relationship of SAPS to storm-enhanced density, *J. Atmos. Sol. Terr. Phys.*, 69, 303–313, doi:10.1016/j.jastp.2006.07.021.

Fuller-Rowell, T. (2011), Storm-time response of the thermosphere–ionosphere system, in *Aeronomy of the Earth's Atmosphere and Ionosphere*, IAGA Spec. Sopron Book Ser., vol. 2, edited by M. A. Abdu and D. Pancheva, pp. 419–434, Springer, Dordrecht, Netherlands, doi:10.1007/978-94-007-0326-1_32.

Galand, M., and A. D Richmond (2001), Ionospheric electrical conductances produced by auroral proton precipitation, *J. Geophys. Res.*, 106(A1), 117–125, doi:10.1029/1999JA002001.

Gkioulidou, M., C.-P. Wang, L. R. Lyons, and R. A. Wolf (2009), Formation of the Harang reversal and its dependence on plasma sheet conditions: Rice convection model simulations, *J. Geophys. Res.*, 114, A07204, doi:10.1029/2008JA013955.

Gkioulidou, M., C.-P. Wang, and L. R. Lyons (2011), Effect of self-consistent magnetic field on plasma sheet penetration to the inner magnetosphere: Rice convection model simulations combined with modified Dungey force-balanced magnetic field solver, *J. Geophys. Res.*, 116, A12213, doi:10.1029/2011JA016810.

Heelis, R. A., J. J. Sojka, M. David, and R. W. Schunk (2009), Storm time density enhancements in the middle-latitude dayside ionosphere, *J. Geophys. Res.*, 114, A03315, doi:10.1029/2008JA013690.

Heinselman, C. J., and M. J. Nicolls (2008), A Bayesian approach to electric field and E-region neutral wind estimation with the Poker Flat Advanced Modular Incoherent Scatter Radar, *Radio Sci.*, 43, RS5013, doi:10.1029/2007RS003805.

Huang, C.-S., J. C. Foster, L. P. Goncharenko, P. J. Erickson, W. Rideout, and A. J. Coster (2005), A strong positive phase of ionospheric storms observed by the Millstone Hill incoherent scatter radar and global GPS network, *J. Geophys. Res.*, 110, A06303, doi:10.1029/2004JA010865.

Kelley, M. C., M. N. Vlasov, J. C. Foster, and A. J. Coster (2004), A quantitative explanation for the phenomenon known as storm-enhanced density, *Geophys. Res. Lett.*, 31, L19809, doi:10.1029/2004GL020875.

Ledvina, B. M., J. J. Makela, and P. M. Kintner (2002), First observations of intense GPS L1 amplitude scintillations at mid-latitude, *Geophys. Res. Lett.*, 29(14), 1659, doi:10.1029/2002GL014770.

Lu, G., L. Goncharenko, M. J. Nicolls, A. Maute, A. Coster, and L. J. Paxton (2012), Ionospheric and thermospheric variations associated with prompt penetration electric fields, *J. Geophys. Res.*, 117, A08312, doi:10.1029/2012JA017769.

Mannucci, A. J., B. D. Wilson, D. N. Yuan, C. H. Ho, U. J. Lindqwister, and T. F. Runge (1998), A global mapping technique for GPS-derived ionospheric total electron content measurements, *Radio Sci.*, 33, 565–582, doi:10.1029/97RS02707.

Mannucci, A. J., B. T. Tsurutani, B. A. Iijima, A. Komjathy, A. Saito, W. D. Gonzalez, F. L. Guarnieri, J. U. Kozyra, and R. Skoug (2005), Dayside global ionospheric response to the major interplanetary events of October 29–30, 2003 "Halloween Storms", *Geophys. Res. Lett.*, 32, L12S02, doi:10.1029/2004GL021467.

Mendillo, M. (2006), Storms in the ionosphere: Patterns and processes for total electron content, *Rev. Geophys.*, 44, RG4001, doi:10.1029/2005RG000193.

Rideout, W., and A. Coster (2006), Automated GPS processing for global total electron content data, *GPS Solutions*, 10(3), 219–228, doi:10.1007/s10291-006-0029-5.

Ruohoniemi, J. M., and K. B. Baker (1998), Large-scale imaging of high-latitude convection with Super Dual Auroral Radar Network HF radar observations, *J. Geophys. Res.*, 103, 20,797–20,811, doi:10.1029/98JA01288.

Shepherd, S. G., and J. M. Ruohoniemi (2000), Electrostatic potential patterns in the high-latitude ionosphere constrained by SuperDARN measurements, *J. Geophys. Res.*, 105, 23,005–23,014, doi:10.1029/2000JA000171.

Skone, S., R. Yousuf, and A. Coster (2004), Performance evaluation of the wide area augmentation system for ionospheric storm events, *J. Global Positioning Syst.*, 3(1–2), 251–258.

Sojka, J. J., M. J. Nicolls, C. J. Heinselman, and J. D. Kelly (2009), The PFISR IPY observations of ionospheric climate and weather, *J. Atmos. Sol. Terr. Phys.*, *71*, 771–785, doi:10.1016/j.jastp.2009.01.001.

Sun, Y.-Y., T. Matsuo, E. A. Araujo-Pradere, and J.-Y. Liu (2013), Ground-based GPS observation of SED-associated irregularities over CONUS, *J. Geophys. Res. Space Physics*, *118*, doi:10.1029/2012JA018103.

Thomas, E. G., J. B. H. Baker, J. M. Ruohoniemi, L. B. N. Clausen, A. J. Coster, J. C. Foster, and P. J. Erickson (2013), Direct observations of the role of convection electric field in the formation of a polar tongue of ionization from storm enhanced density, *J. Geophys. Res. Space Physics*, *118*, 1180–1189, doi:10.1002/jgra.50116.

Tsurutani, B. T., et al. (2004), Global dayside ionospheric uplift and enhancement associated with interplanetary electric fields, *J. Geophys. Res.*, *109*, A08302, doi:10.1029/2003JA010342.

Tsurutani, B. T., A. J. Mannuccci, O. P. Verkhoglyadova, and G. S. Lakhina (2013), Comment on "Storming the Bastille: The effect of electric fields on the ionospheric *F*-layer" by Rishbeth et al. (2010), *Ann. Geophys.*, *31*, 145–150, doi:10.5194/angeo-31-145-2013.

Zhang, Q.-H., et al. (2013), Direct observations of the evolution of polar cap ionization patches, *Science*, *339*, 1597–1600, doi:10.1123/science.1231487.

Zou, S., L. R. Lyons, M. J. Nicolls, C. J. Heinselman, and S. B. Mende (2009a), Nightside ionospheric electrodynamics associated with substorms: PFISR and THEMIS ASI observations, *J. Geophys. Res.*, *114*, A12301, doi:10.1029/2009JA014259.

Zou, S., L. R. Lyons, C.-P. Wang, A. Boudouridis, J. M. Ruohoniemi, P. C. Anderson, P. L. Dyson, and J. C. Devlin (2009b), On the coupling between the Harang reversal evolution and substorm dynamics: A synthesis of SuperDARN, DMSP, and IMAGE observations, *J. Geophys. Res.*, *114*, A01205, doi:10.1029/2008JA013449.

Zou, S., L. R. Lyons, and Y. Nishimura (2012), Mutual evolution of aurora and ionospheric electrodynamic features near the Harang reversal during substorms, in *Auroral Phenomenology and Magnetospheric Processes: Earth and Other Planets*, Geophys. Monogr. Ser., vol. 197, edited by A. Keiling et al., pp. 159–169, AGU, Washington, D. C., doi:10.1029/2011GM001163.